Chemical Engineering Science 324 (2026) 123260

Contents lists available at ScienceDirect

Chemical Engineering Science

journal homepage: www.elsevier.com/locate/ces

Particle-pore scale study of the expansion and minimum fluidization of fine particles

Qiong Wu [a], Yi Zou [b,*], Yongli Wu [c], Jing He [d]

[a] College of Automation, Nanjing University of Posts and Telecommunications, Nanjing 210023, PR China
[b] Department of Chemical and Biological Engineering, Monash University, Clayton, VIC 3168, Australia
[c] Faculty of Civil Engineering & Geosciences, Delft University of Technology, 2628 CN Delft, the Netherlands
[d] School of Computer Science, Nanjing University of Posts and Telecommunications, Nanjing 210023, PR China

ARTICLE INFO

Keywords:
Particle-pore scale
Expanded fluidization
Minimum bubbling velocity
Particle-fluid flow
Fine particles

ABSTRACT

A coupled approach combining the Discrete Element Method (DEM) and the Pore Network Model (PNM) is developed to simulate particle-fluid flows at equivalent solving scales, specifically, the particle scale via DEM for capturing solid-phase dynamics, and the pore scale via PNM for characterizing fluid flow. Initially, the DEM-PNM model yields results that are largely consistent with those of the DEM-Lattice Boltzmann Method (DEM-LBM) in simulating a dynamic cell under low Reynolds number conditions. Subsequently, the model is employed to replicate the formation of a stable expanded bed composed of fine particles. By analyzing pore-scale fluid flow, tortuous flow paths, and particle-particle force chains, the results reveal that the development of a stable expanded bed corresponds with microscopic structural evolutions that reduce resistance to gas flow and enhance mechanical stability. Finally, leveraging the micromechanical interactions at the particle and pore scales, a quantitative correlation is derived to predict the minimum bubbling velocity of fine cohesive particles. This correlation explicitly incorporates particle-scale properties, including the Hamaker constant, as well as pore structure characteristics within the particle assembly. Overall, the study demonstrates that the DEM-PNM approach, operating at an equivalent particle-pore scale, holds significant promise for advancing the understanding of particle-fluid flow micromechanics.

1. Introduction

Particle-fluid flows are prevalent in various industrial applications, including fluidized bed reactors, hydro-cyclones, and pneumatic conveying systems (Shi and Sakai, 2022). These phenomena are inherently complex, exhibiting spatial and temporal behaviours across multiple scales (Chen et al., 2022; Ji et al., 2023; Wang and Shen, 2022b). Such complexity poses significant challenges in the scale-up and control of these processes, often leading to operational uncertainties. With advancements in computational technologies, numerical simulation has emerged as a powerful tool for capturing the detailed spatiotemporal dynamics of particle-fluid systems, offering promising potential for improving the design, optimization, and control of industrial processes.

Over the past few decades, numerous numerical approaches have been developed to simulate particle-fluid flows (Ge et al., 2019; Sundaresan et al., 2018; van der Hoef et al., 2008; Zhu et al., 2007). Among these, methods based on the Discrete Element Method (DEM) (Cundall and Strack, 1979) are particularly notable for their ability to track the motion of individual particles and explicitly account for particle-particle interactions without relying on constitutive equations. DEM-based approaches can generally be classified into two main categories, distinguished by the method used to compute the fluid phase. The first category is represented by the coupled Computational Fluid Dynamics and DEM (CFD-DEM) approaches (Amritkar et al., 2014; Kloss et al., 2012; Liu et al., 2013). In CFD-DEM, the fluid phase is resolved using computational cells that are typically larger than the particles themselves, with particle-fluid interactions calculated based on cell-scale averaged porosity and fluid flow fields. CFD-DEM has been widely adopted for simulating particle-fluid systems (Wang and Shen, 2021a, 2021b; Yue et al., 2021). However, a key limitation is the inconsistency in the spatial resolution between the solid and fluid phases: while the solid phase is resolved at the particle scale, the fluid phase is computed at a coarser, cell-based scale. This mismatch can introduce uncertainties in the calculation of particle-fluid interactions. For example, drag forces

* Corresponding author.
E-mail address: yi.zou@monash.edu (Y. Zou).

https://doi.org/10.1016/j.ces.2025.123260
Received 3 October 2025; Received in revised form 18 December 2025; Accepted 26 December 2025
Available online 28 December 2025

on individual particles are derived from averaged fluid properties at the cell level, making it challenging to capture the influence of local structural heterogeneity within the cell (Wang and Shen, 2022a). Recent efforts have sought to address this issue by developing structure-dependent drag correlations based on direct numerical simulations (Liu et al., 2020; Ma et al., 2020). Nevertheless, due to the diverse structural characteristics inherent in particle-fluid flows, extensive validation of these correlations remains necessary. The second category of approaches employs direct numerical simulation (DNS) to resolve the fluid phase at sub-particle scales, while still modelling the solid phase at the particle scale using the DEM. This category includes methods such as the lattice Boltzmann method (LBM) (Fei et al., 2023; Fu et al., 2024; Fu and Wang, 2023; Jiang et al., 2022; Tsigginos et al., 2022) and smoothed particle hydrodynamics (SPH) (Bu et al., 2022; Jo et al., 2022; Xu et al., 2022; Zhou et al., 2022; Zou et al., 2022), which can be configured to perform DNS. Compared to traditional unresolved CFD-DEM methods, sub particle approaches offer higher accuracy and capture more detailed physical phenomena. However, because they resolve the fluid at scales much smaller than individual particles, these methods are computationally expensive and typically limited to small simulation domains.

The mismatch in computational scales between the fluid and solid phases in existing approaches can either hinder the accurate determination of particle-fluid interaction forces, as in CFD-DEM, or incur substantial computational costs, as in DNS-DEM. This highlights the need for simulation methods that operate at equivalent resolving scales for both phases. Compared to CFD, the Pore Network Model (PNM) (Blunt, 2001; Bryant et al., 1993; Thompson and Fogler, 1997) offers a more efficient means of capturing the essential structural features and fluid flow behavior at the pore scale within particle assemblies. Importantly, PNM can be coupled with DEM to simulate dynamic particle-fluid flows at equivalent solving scales, specifically, using the particle scale for the solid phase and the pore scale for the fluid phase. In this coupled DEM-PNM framework, fluid flow occurs through tortuous pore networks formed by the particle assemblies, exerting forces on individual particles. As the particles respond to these forces and change position, the geometry of the pore network evolves, in turn altering the fluid flow. Early investigations of the DEM-PNM approach were primarily conducted in two-dimensional (2D) systems (Bruno, 1994; Jain and Juanes, 2009; Zhang et al., 2013). More recently, studies have extended this methodology to three-dimensional (3D) systems. Notably, Chareyre et al. (2011) formally derived equations for calculating particle-fluid interaction forces within a PNM framework. Catalano et al. (2014) demonstrated the ability of the pore scale model to capture strong poromechanical effects. while Yang and Juanes (2018) investigated the effect of pore pressure on fault slip behaviors. However, the majority of these DEM-PNM applications have been confined to the field of geomechanics (Giudici et al., 2023; Sufian et al., 2019; Zhao et al., 2023). Recent years have seen transformative progress in PNM for fluid-solid coupling, extending its application from static permeability calculations to dynamic, multiscale, and machine-learning-enhanced frameworks. For instance, NeuroPNM introduced by Jendersie et al. (2024) represents a significant shift toward model reduction, using neural networks to extract macroscopic transport coefficients from high-resolution PNM simulations of reacting particle systems. In the context of geo-mechanics, Li et al. (2022) developed a grain-based DEM-PNM coupling to simulate hydraulic fracturing in polymineralic rocks, successfully capturing the transition between intergranular and intragranular fractures, a level of detail that traditional CFD-DEM struggles to achieve. Furthermore, the integration of PNM with larger-scale solvers has gained momentum. Cao et al. (2025) proposed an anisotropic CFD-DEM-PNM coupling method to simulate soil-rock erosion, deriving a mapping between micro-scaled pore-pipe conductance and macro-scaled permeability tensors. Meanwhile, multiscale constructions for granular soils have improved the accuracy of two-phase flow simulations by accounting for the heterogeneous pore topology (Mufti and Das, 2023). While these works have pushed the boundaries of PNM in rock mechanics and reactor engineering, their focus often remains on quasi-static grain structures or macro-scale erosion. Our work distinguishes itself by applying a fully dynamic, particle-scale DEM-PNM coupling specifically to the fluidization and bubbling of fine cohesive powders.

In chemical engineering, the gas fluidization of fine particles plays a crucial role in a variety of processes, including fluid catalytic cracking, methanol-to-olefins conversion, and coal combustion. Due to the presence of interparticle forces, such as van der Waals forces, the behaviour of fine particles can differ significantly from that of coarse particles. For instance, when the gas velocity exceeds the minimum fluidization velocity u_{mf}, a bed of fine particles does not immediately exhibit bubbling behaviour as in the case of coarse particles. Instead, it initially undergoes expansion, forming a stable expanded bed before reaching the minimum bubbling velocity u_{mb}, which is typically higher than u_{mf}. The formation of expanded beds and the transition to bubbling fluidization have been extensively studied over the past decades through both experimental (Foscolo and Gibilaro, 1984; Geldart, 1973; Guo et al., 2018; Gupta and De, 2022; Menon and Durian, 1997; Valverde et al., 2003) and numerical approaches (Gan et al., 2019; Hou et al., 2012; Rhodes et al., 2001; Thornton et al., 2015; Wang et al., 2010; Wang et al., 2023; Ye et al., 2004). It is generally acknowledged that both interparticle cohesive forces and hydrodynamic forces contribute to the formation of the expanded bed. In particular, particle-particle contacts have been a focus of study for understanding the mechanical stability of the bed structure (Hou et al., 2012; Thornton et al., 2015). However, the role of pore-scale fluid flow among particle, an important factor in the bed's stability and the onset of bubbling, has received relatively limited attention. Furthermore, while numerous empirical and semi-empirical correlations have been proposed for predicting the minimum bubbling velocity u_{mb} of fine particles, discrepancies often remain when these models are compared with experimental data (Oke et al., 2015). A likely reason for these deviations is the insufficient incorporation of particle-scale micromechanics in the derivation of such correlations. For example, although it is well established that particle cohesion significantly influences u_{mb} (Rhodes et al., 2001), existing correlations do not explicitly include cohesion parameters in their formulations.

In this study, a coupled Discrete Element Method-Pore Network Model (DEM-PNM) approach is developed and applied to investigate gas fluidization behaviour in beds of fine particles. The model is first validated through comparison with results from DEM-Lattice Boltzmann Method (DEM-LBM) simulations. Subsequently, the DEM-PNM framework is used to simulate the formation of an expanded bed, enabling detailed characterization of the micromechanical interactions at the particle and pore scales. This includes analysis of fluid flow pathways, force chains, and pore structure evolution during the expansion process. Finally, based on the micromechanical insights obtained, a quantitative correlation is derived to predict the minimum bubbling velocity u_{mb} of fine particles, incorporating particle-scale and pore-scale properties.

2. Model description

2.1. DEM-PNM approach

For DEM-PNM approach, the solid flow is described by DEM, originally proposed by Cundall and Strack (1979). Each particle possesses both translational and rotational motions, which are governed by Newton's second law of motion. The governing equations are written as (Zhu et al., 2007):

$$m_i\frac{d\mathbf{v}_i}{dt}=\sum_j\left(\mathbf{F}_{e,ij}+\mathbf{F}_{d,ij}+\mathbf{F}_{v,ij}\right)+m_i\mathbf{g} \tag{1}$$

$$I_i\frac{d\omega_i}{dt}=\sum_j\left(\mathbf{T}_{t,ij}+\mathbf{T}_{r,ij}\right) \tag{2}$$

where m_i, $\mathbf{v}_i$, $\boldsymbol{\omega}_i$ and I_i are the mass, translational and rotational

velocities, and the moment of inertia of particle i. Here, the forces involved include particle-fluid interaction force $\mathbf{F}_{pf,i}$, the gravitational force $m_i\mathbf{g}$ and the forces between particles (and between particles and walls) which include the elastic force $\mathbf{F}_{e,ij}$, viscous damping force $\mathbf{F}_{d,ij}$ and cohesive van der Waals force $\mathbf{F}_{v,ij}$. The van der Waals force is given by (Hamaker, 1937):

$$\mathbf{F}_{v,ij} = -\frac{H_a}{6}\times\frac{64R_i^3R_j^3\left(h+R_i+R_j\right)}{\left(h^2+2R_ih+2R_jh\right)^2\left(h^2+2R_ih+2R_jh+4R_iR_j\right)^2}\mathbf{n}_{ij} \tag{3}$$

where H_a is the Hamaker constant, and h is the separation of surfaces along the line of the centers of particles i and j. To avoid singular attractive force when h equals to zero, a minimum separation h_{min} is assumed. The torque acting on particle i due to particle j includes two components: $\mathbf{T}_{t,ij}$ which is generated by the tangential force and $\mathbf{T}_{r,ij}$ which is known as the rolling friction torque. If a particle i undergoes multiple interactions, the individual interaction forces and torques are summed up for all particles interacting with it. The computation equations of these forces and torques can be found in our previous work (Wu et al., 2017; Yang et al., 2000).

The fluid flow is described by the pore network model (Blunt, 2001; Bryant et al., 1993; Thompson and Fogler, 1997; Wu et al., 2019). As shown in Fig. 1, the pore units are obtained based on the Delaunay tessellation of the particle centers. Here, A_{ij}^f is the area of the fluid part $S_{ij}\cap\Theta$ of facet ij, where Θ represent the pore space, S_{ij} is the surface of the facet ij, separating tetrahedra i and j. Area A_{ij}^k is the area of the intersection $S_{ij}\cap\Gamma_k$, Γ_k is the domain occupied by solid particle k. Then, the mass and momentum balances are established on each pore unit. The mass balance equation is written as:

$$\sum_{j=1}^{4}q_{ij} = \sum_{1}^{4}\int_{S_{ij}}(u-v)\cdot n ds = -\frac{\partial V_i}{\partial t} \tag{4}$$

which indicates that the fluid flows in and out of the four faces of each pore is equal to the rate of pore volume change (resulted from the dynamic movement of particles). q_{ij} is the volumetric flow rate between pore i and j, $\mathbf{u}$ and $\mathbf{v}$ are the velocities of the fluid and particle, respectively. $\mathbf{n}$ is the local normal vector of S_{ij}, V_i is the volume of the pore unit i, and $\partial V_i/\partial t$ is the rate of change in pore volume over time. It is assumed that the bed undergoes a quasi-static expansion before the onset of bubbling. Hence, the continuity equation can be simplified to $\sum_{j=1}^{4}q_{ij} = 0$. Note that the fluid flux at each face q_{ij} is the integral of the relative velocity between fluids and the solid particles. And the momentum equation is written as:

$$P_i - P_j = \frac{32\mu L_{ij}}{D_{ij}^{*2}}U_{ij} + \frac{\rho_f L_{ij}}{2D_{ij}^{*}}U_{ij}^2 \tag{5}$$

The first and second terms at the right hand represents the viscous and inertial effects, respectively; $U_{ij} = q_{ij}/S_{ij}$, which is the flow velocity between pore i and pore j, P_i and P_j are the pressure of pore i and pore j, respectively, μ is the dynamic viscosity, ρ_f is the fluid density, D_{ij} is modified as D_{ij}^* by a shape factor (Thompson and Fogler, 1997). The Thompson's conduction model was selected based on its proven accuracy in the literature for the specific porosity range investigated in this study. Recent comparative studies, such as that by Rong et al. (2020), have demonstrated that within the porosity range relevant to our current study, the Thompson's model provides permeability predictions that exhibit only negligible deviation when compared to more computationally intensive, fully resolved CFD-based models.

The packed bed now can be represented as a collection of interconnected pore units, within which mass and momentum conservation equations can be formulated. Once the boundary conditions of the system are specified, these governing equations can be solved simultaneously to determine the fluid flow characteristics throughout the pore network. To further enhance computational efficiency and ensure robust convergence for the resulting large sparse linear systems, the parallel PARDISO solver was employed in this work. The detailed solving procedure for the equations can be found in our previous work (Wu et al., 2019).

At a pore scale, fluid experiences a pressure loss ΔP_{ij} when it flows through a pore throat ij (connecting pores i and j). Basically, ΔP_{ij} is mainly resulted from two particle-fluid interaction forces (Chareyre et al., 2011), i.e., $\mathbf{F}_{p,ij}$ induced by pressure gradient and $\mathbf{F}_{d,ij}$ due to local viscous drag. Based on the force balance, $\mathbf{F}_{p,ij}$ and $\mathbf{F}_{d,ij}$ can be calculated:

$$\mathbf{F}_{p,ij} = A_{s,ij}\Delta P_{ij}\mathbf{n}_{ij} \tag{6}$$

$$\mathbf{F}_{d,ij} = A_{f,ij}\Delta P_{ij}\mathbf{n}_{ij} \tag{7}$$

where $A_{s,ij}$ and $A_{f,ij}$ are the solid and fluid part of the interface, respectively; and $\mathbf{n}_{ij}$ is the unit vector pointing from the centre of pore i to that of pore j. A particle may be surrounded by several pore throats, and the total particle-fluid force $\mathbf{F}_{pf}$ on a particle is the sum of $\mathbf{F}_{p,ij}$ and $\mathbf{F}_{d,ij}$ from all neighbouring throats. More details on the allocation of particle-fluid force from throat to particles can be found in previous studies (Chareyre et al., 2011; Wu et al., 2019).

The coupling scheme of the present approach is implemented in an explicit and sequential manner (Fig. 2). At each time step, particle contacts are first identified based on the current particle positions. The

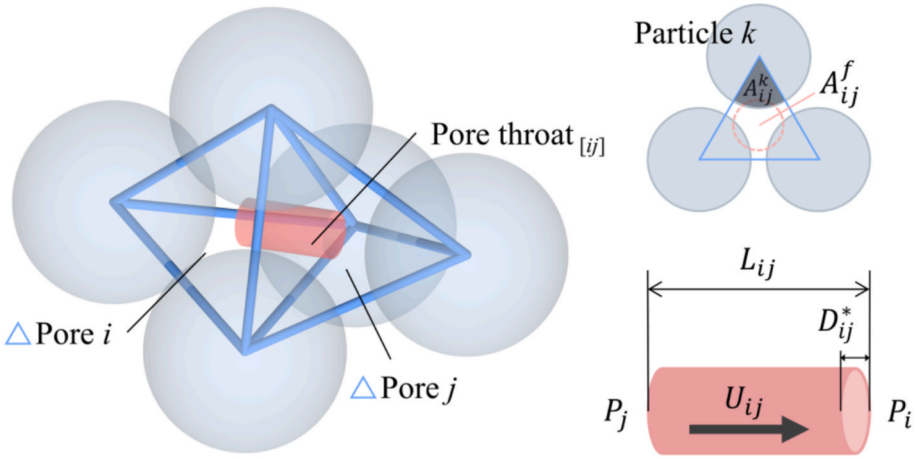

Fig. 1. Schematic of pore network model: a pore unit and pore–pore connection.

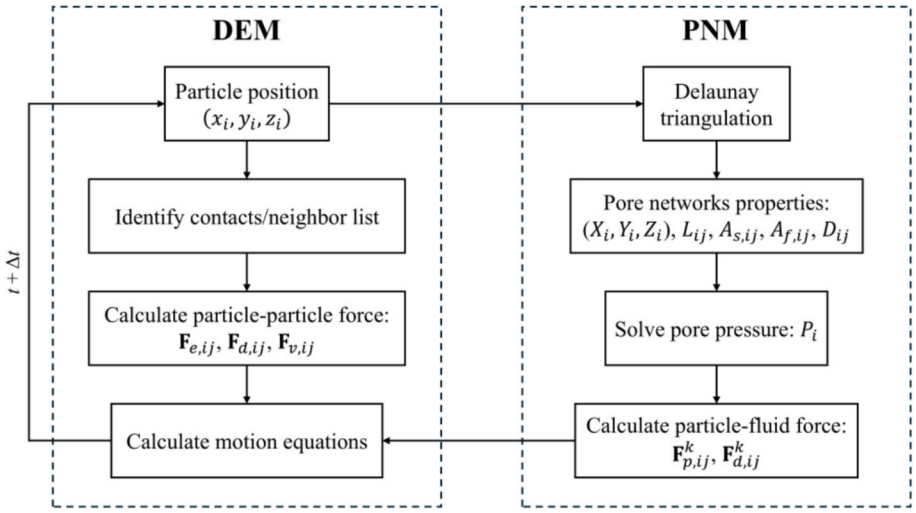

Fig. 2. Flow chart of DEM-PNM coupled modelling.

corresponding particle-particle interaction forces are then computed using a contact law applied to each contacting pair. Simultaneously, the pore geometry is dynamically reconstructed based on the instantaneous particle arrangement. This ensures that the pore-scale flow resistance and the resulting particle-fluid interaction forces evolve synchronously with the varying particle spacing and throat dimensions. These newly calculated particle-particle and particle-fluid forces are subsequently used to update the positions and velocities of the particles. The updated particle positions and velocities then form the basis for recalculating contact interactions and pore-scale fluid flows in the following time step, thereby completing the coupling loop.

2.2. Boundary conditions in fluidization

To enforce the no-slip boundary condition at the sidewalls of the fluidized bed, "infinite-sized" spheres are placed along each wall. The spatial tessellation of these boundary spheres is performed using radical tessellation (Rycroft, 2009), which ensures that the resulting pore throats consistently pass through the void space rather than intersecting the solid phase. This approach is analogous to the regular tessellation implemented via the CGAL library (Boissonnat et al., 2002) in the work of Chareyre et al. (2011).

In a fluidized bed, both dense and dilute particle zones coexist. Nonetheless, pore networks can still be effectively constructed using Delaunay and Voronoi tessellation techniques, as illustrated in Fig. 3. The open-source library VORO++ (Rycroft, 2009) is employed to facilitate this process, enabling surface meshing by initializing a small polyhedron around each particle. Occasionally, a few pore units near the top of the bed may exhibit unusually large sizes. However, since the pressure at these top boundary pores is typically set to zero, their impact on the fluid flow within the interior of the bed is negligible. For particles located in these boundary pores, particle-fluid interaction forces are computed separately using empirical models from CFD-DEM (Rong et al., 2013), which rely on the locally averaged fluid flow.

Gas is injected uniformly from the bottom of the bed at a prescribed superficial velocity. To achieve this target gas velocity at the i-th simulation time step, a pressure difference ΔP_i^* is set at the top ($P_{i,top} = 0$) and bottom ($P_{i,bottom} = \Delta P_i^*$) of the bed; the specific value of ΔP_i^* is determined iteratively, as shown in Fig. 4. Each iteration begins by initializing the pressure difference using the value from the previous time step (ΔP_{i-1}^*). The pressure update incorporates a relaxation factor ($\delta = 0.5$ in this study) to ensure numerical stability and convergence. This iterative control scheme is analogous to the method used by Al-Gharbi and Blunt (2005) for achieving constant flow flux in porous media.

3. Results and discussion

3.1. Model validation

In our previous study, the predictive capability of the PNM for fluid flow was validated against experimental measurements of bed permeability, in dense packed beds (Wu et al., 2019). To rigorously validate the DEM-PNM model, the fluidization of particles is realized and compared against established experimental data. Here the gas is uniformly introduced from the bottom of the particle bed, as illustrated in Fig. 5(a), the simulation settings are identical to those used in

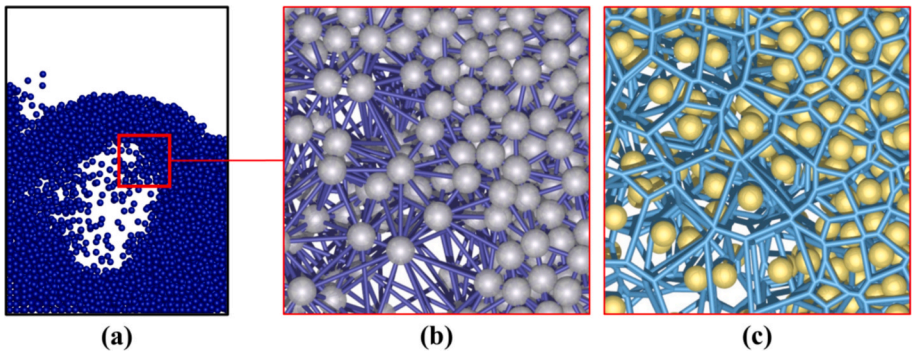

Fig. 3. Meshing for a fluidized bed: (a) original bed; (b) meshing with Delaunay tessellation and (c) meshing with Voronoi tessellation.

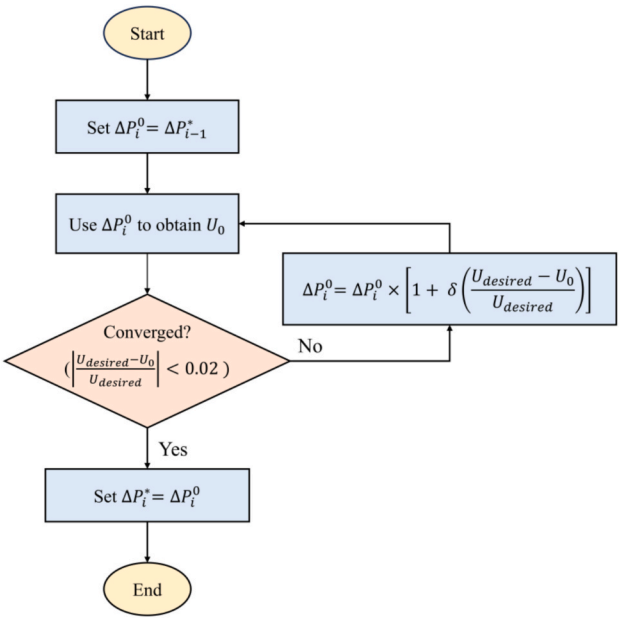

Fig. 4. Flowchart for the determination of ΔP_i^* to obtain a constant flow rate.

experiment (Tang et al., 2016) for further validation. The initial location of the particle is fixed, and inlet and outflow boundary pressure conditions are enforced on the bottom and top pores. A key objective of this study is to validate the proposed model by delineating the relationship between the bed's pressure drop and the superficial gas velocity. The latter is conceptualized as the total volumetric flow rate of gas normalized by the bed's cross-sectional area, serving as a proxy for the gas jet velocity. The pressure difference across the bed, represents the differential in gas pressure from the bottom to the top of the bed, measured along its symmetrical axis. Fig. 5(b) gives the relationship between superficial gas velocity U and bed pressure drop ΔP by gradually increasing the superficial gas velocity. Here, the superficial velocity is converted from the average volumetric flow rate divided by the cross-sectional area of the entire bed; ΔP is the time-averaged pressure difference between the two ends of the particle bed. As can be observed from the curves, the results by the PNM-LBM-DEM approach are quantitively in good agreement with that obtained from the experiment for different number densities of virtual particles. The predicted minimum fluidized velocity of 1.36 m/s is very close to 1.29 m/s which is estimated using Wen and Yu (1966)'s correlation.

For further validation, the particle-fluid flows simulated by the present DEM-PNM model in a cubic cell with periodic boundary conditions (PBC) are compared against results obtained using the DEM–Lattice Boltzmann Method (DEM-LBM). The LBM mesh resolution was set to 40 grid units per particle diameter ($\Delta x = d_p/40$) to ensure stability and accurately resolve the flow in the interstitial spaces of the packed bed. The LBM-DEM approach has been previously validated by comparing the predicted drag coefficient for an isolated particle in power-law fluids against the experimental measurements, with the prediction errors consistently found to be less than 4.2 % (Qi et al., 2018).

As illustrated in Fig. 6, the simulation domain is a cube with dimensions of 7.5 d_p × 7.5 d_p × 7.5 d_p, where d_P denotes the particle diameter, set to 0.01 m in this study. PBCs were applied to the particles in all directions and the pore network in the horizontal (X and Y) directions. Crucially, the vertical direction (Z, flow direction) was treated as non-periodic for the pore network. A fixed pressure gradient was imposed by setting different constant pressure values at the non-periodic top and bottom boundaries. To achieve a quasi-steady state for the particle-fluid system, consistent with previous DEM-LBM simulations (Qi et al., 2019), a suitable pressure difference is imposed between the top and bottom boundaries, ensuring a balance between the gravitational force acting on the particles and the opposing particle-fluid interaction forces, thereby stabilizing the system for comparison.

As described above, particles in the simulation reach a quasi-steady state under the opposing influences of gravitational and particle-fluid forces. Although the overall particle assembly is in equilibrium with no net acceleration, individual particles exhibit dynamic behaviour characterized by fluctuating velocities, defined as $v_p' = (v_p - \langle v_p \rangle)/\langle v_p \rangle$, due to variations in local structure and fluid flow. The distribution of particle velocity fluctuations is shown in Fig. 7. The results demonstrate a strong agreement between the present DEM-PNM model and the DEM-LBM simulations, particularly at low Reynolds numbers (Re). However, at higher Reynolds numbers (e.g., Re = 100), the agreement deteriorates. This discrepancy is likely attributable to limitations in

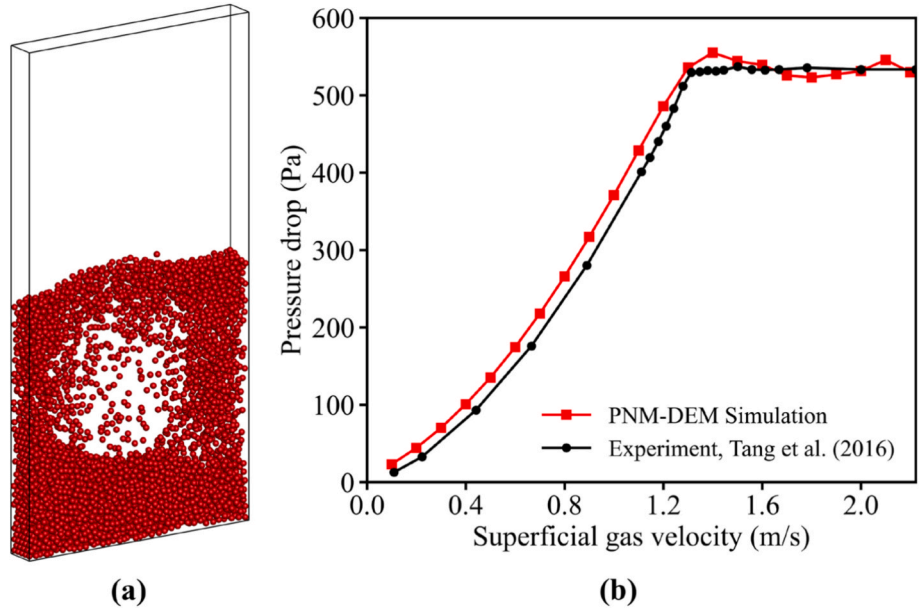

Fig. 5. (a) Schematic representation of gas-fluidized bed; (b) bed pressure drop vs superficial gas velocity curves obtained by PNM-DEM and experiment measurement from literature.

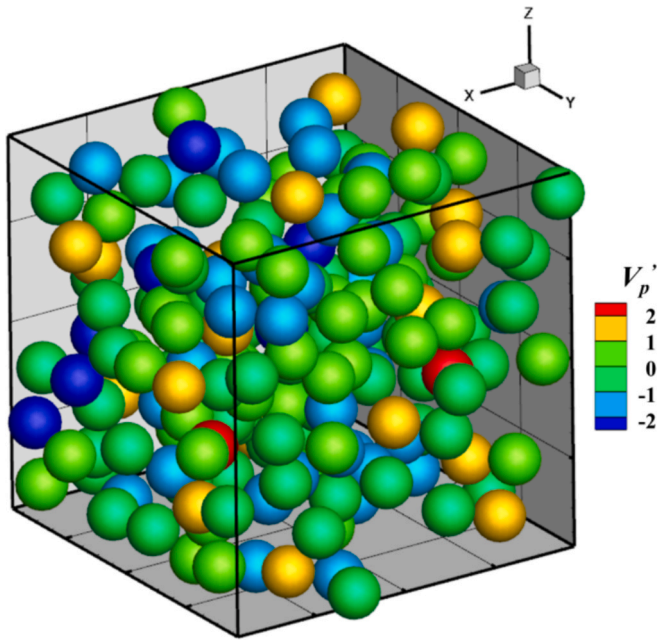

Fig. 6. Particle dynamics in a cell with periodic boundary condition.

accurately capturing the relative motion between particles and fluids. As indicated in the governing equations (e.g., *Eq. (3)*), the relative velocity between particles and fluid, $(\mathbf{u}-\mathbf{v})$, must be evaluated at each pore throat. Since each pore throat is bounded by three particles, the particle velocity used in the calculation is approximated as the average velocity of the three surrounding particles. This averaging approach is more valid under conditions of low porosity and low Reynolds number, where the velocities of neighbouring particles are likely to be similar. In contrast, under high porosity and high Re conditions, significant velocity differences may exist among the three bounding particles, rendering the averaged velocity a poor approximation of local dynamics. Consequently, this introduces errors in the estimation of relative velocities and, therefore, in the computed particle-fluid forces. In light of this, caution is warranted when applying the DEM-PNM model to dilute or fast-flowing systems. In the present study, the gas fluidization of fine particles is examined strictly under low Reynolds number conditions ($Re < 1$) to ensure model accuracy.

In addition, the predictive capability of the PNM for fluid flow was previously validated against experimental measurements of bed permeability, in dense packed beds (Wu et al., 2019). The calculated permeabilities for beds composed of different particle diameters showed excellent quantitative agreement with experimental data, establishing the fidelity of the model's hydrodynamic component.

3.2. Formation of a stable expanded bed

The simulation parameters are summarized in Table 1. The Young's modulus used in simulation is a reduced stiffness to accelerate computation. Poisson's ratio, sliding and rolling friction coefficients are adopted from literature values (Tang et al., 2019) that have been calibrated by experiments. The inlet gas velocity is set to 1.5 cm/s, corresponding to a Re below 1. Under these conditions, viscous forces dominate the particle-fluid interactions. The material properties assigned to the particles and gas are representative of glass beads and air, respectively. To reduce computational cost, the bed thickness is limited to 3 d_P. As a result, PBC are applied in the front and rear directions to mimic a quasi-infinite system in those dimensions.

Snapshots illustrating the evolution of particle flow patterns during the formation of a stable expanded bed are presented in Fig. 8. Gas is introduced from the bottom of the initially packed bed, initiating fluidization and resulting in the formation of dynamic bubbles within

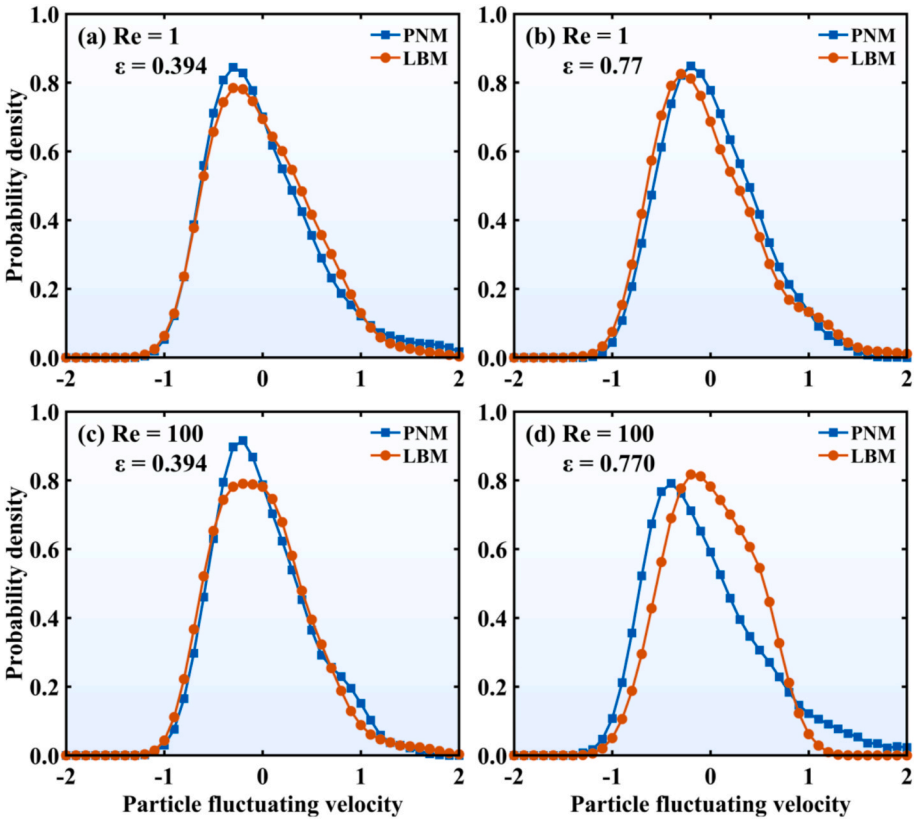

Fig. 7. Probability distribution of particle fluctuating velocity.

Table 1
Parameters used in the expanded fluidization of glass bead.

Parameters	Values
Particle size, d_p	96 μm
Particle number, n_p	3,500
Particle density, ρ_p	2460 kg m^{-3}
Gas viscosity, μ_f	1.8 × 10^{-5} kg m^{-1} s^{-1}
Gas density, ρ_f	1.25 kg m^{-3}
Hamaker constant, H_a	6.5 × 10^{-21} J
Minimum separation, h_{min}	1 nm
Sliding friction coefficient, μ_s	0.2
Rolling friction coefficient, μ_r	0.01
Young's modulus, E	1.0 × 10^{7}N m^{-2}
Poisson's ratio, υ	0.25
Bed width, x	36 d_p
Bed thickness, y	3 d_p
Inlet gas velocity, u_f	1.5 cm/s
Time step, Δt	0.2 × Rayleigh time step

the particle assembly. This transient fluidization phase persists for less than 0.5 s, after which the system undergoes a defluidization process characterized by a gradual dissipation of particle velocity. By $t = 1.0$ s, a stable expanded bed is established, exhibiting negligible particle motion and no significant structural rearrangements.

The temporal evolution of bed porosity ϵ and pressure drop ΔP is shown in Fig. 9. The pressure drop is presented in a dimensionless form, defined as $\Delta P = (P_{in} - P_{out})/(W_{bed}/A_{bed})$, where P_{in} and P_{out} denote the inlet and outlet pressures, respectively; W_{bed} is the total weight of the bed; and A_{bed} is the cross-sectional area of the bed. In the initial phase (0–0.2 s), porosity increases while pressure drop decreases, corresponding to the onset of particle fluidization (see Fig. 8). Subsequently, between 0.2 s and 0.5 s, the bed undergoes partial defluidization, marked by a slight reduction in porosity and a corresponding increase in pressure drop. After 0.5 s, both porosity and pressure drop stabilize, indicating the establishment of a stable expanded bed.

The distribution of pore pressures at different instants is given in Fig. 10. Generally, pore pressure varies almost linearly with the bed height for both the packed ($t = 0$ s) and expanded beds ($t = 0.2$ s or $t = 1.0$ s). Nevertheless, compared with the packed bed, pore pressure at the

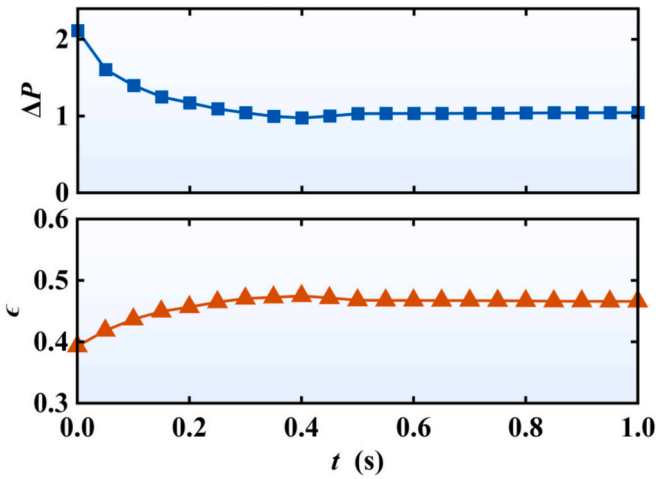

Fig. 9. Evolution of porosity and dimensionless pressure drop of the bed with time.

expanded bed is much decreased with a smaller slope for the pressure – height relationship. This can be ascribed to the decreased frictional resistance of the expanded bed with increased bed porosity. Besides, the pressure distributions at $t = 0.2$ s and $t = 1.0$ s are largely similar. However, at $t = 0.2$ s, the pore pressures in the upper region of the bed are more scattered (Fig. 10(b)), indicating there is a larger pressure gradient even at the same bed height. Such pressure gradient can result in the microscopic structural evolution of the bed and will be discussed in the following content.

The fluid flows at pore throats are visualized in Fig. 11. Compared with the fluid flow in packed bed, fluid flow in expanded bed is less uniform, possibly due to the less uniform structure with large pores. Besides, it is noted that local differences are observed for the flow distributions at $t = 0.2$ s and $t = 1.0$ s, as indicated by the enlarged view for a same location. Especially, fluid flows with larger velocities (red ones) are appeared at $t = 1.0$ s. This indicates that microscopic structural evolution exists from $t = 0.2$ s to $t = 1.0$ s, even the macroscopic bed

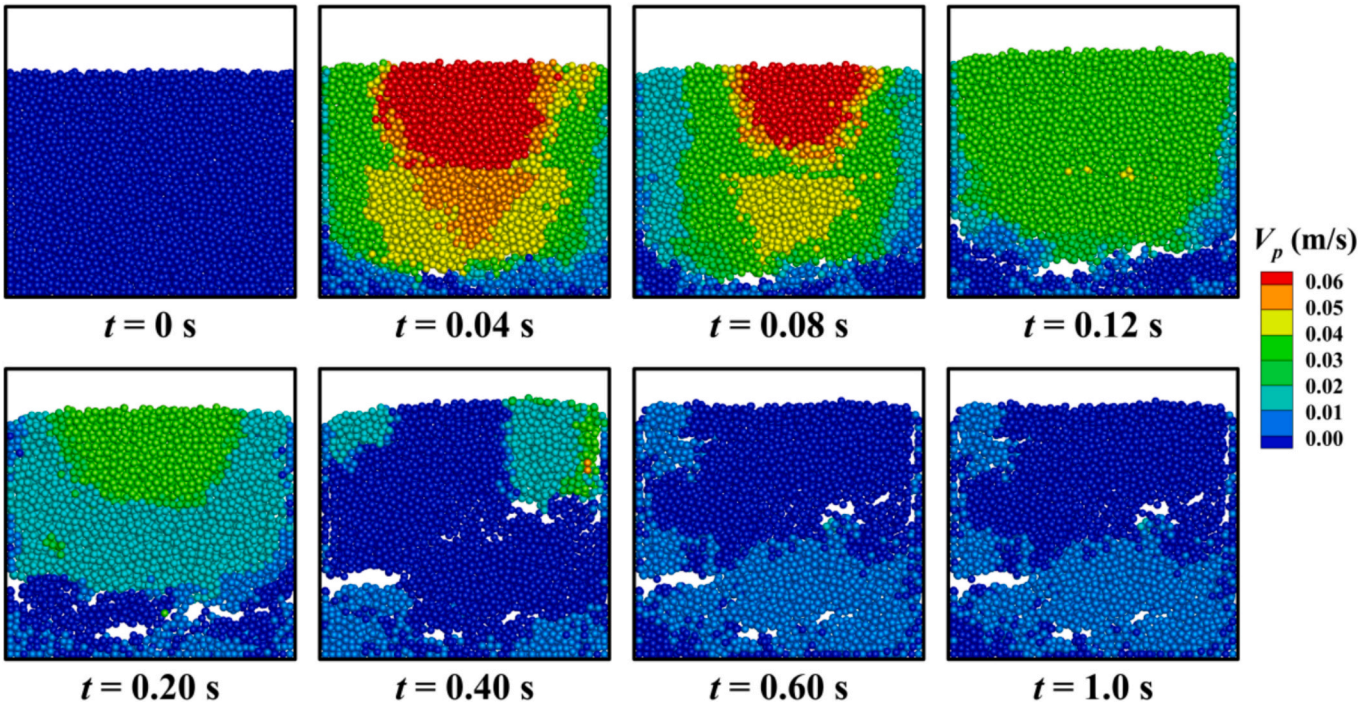

Fig. 8. Flow patterns in the formation of a stable expanded bed.

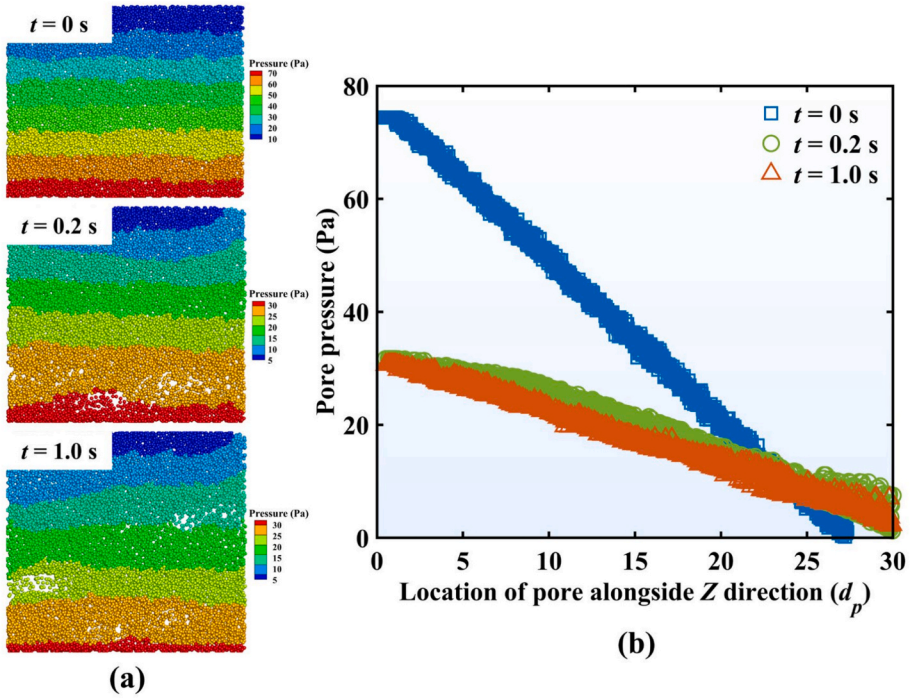

Fig. 10. Distribution of pore pressures, where each sphere in (a) represents a pore unit.

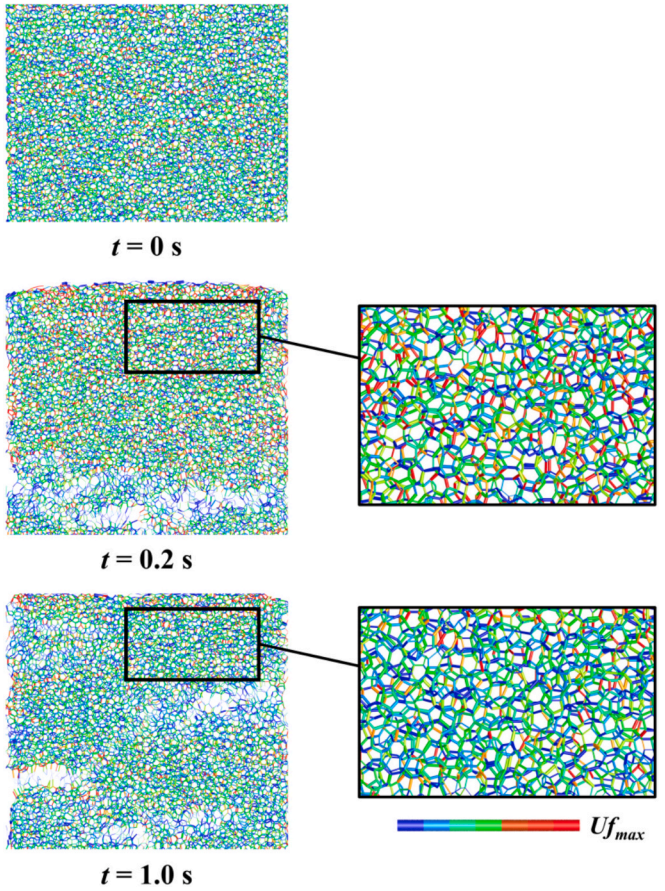

Fig. 11. Distribution of pore scale fluid flows, where each stick represents a pore throat and the stick colour indicates the velocity of the fluid flow.

properties like the overall porosity and pressure drop are almost kept the same (Fig. 9).

To further understand the microscopic change of the bed structure, typical flow paths and tortuosity of the bed are characterized (Fig. 12). Such torturous flow paths connect a series of neighbouring pore units from the bed bottom to the top, and are determined through searching the shortest paths by using a recursive depth-first search algorithm. The tortuosity L_e is defined as the ratio of the lengths of the actual flow path L_{actual} and the height of the bed L_0, i.e., $L_e = \frac{L_{actual}}{L_0}$.

Normally, a small tortuosity indicates a small frictional resistance of the structure to fluid flow. At each instant of time, six flow paths are found in the bed with their tortuosity averaged. As shown in Fig. 12(b), the initial tortuosity decreases significantly when the bed is fluidized at $t = 0.1$ s, but it increases when the bed is defluidized to form the expanded bed ($t = 0.2$ s). Specifically, the flow path at $t = 0.2$ s can be obviously torturous in the upper region of the bed (see the purple path at $t = 0.2$ s in Fig. 12(a)), accounting for the relatively small fluid velocity shown in Fig. 10. Then, tortuosity gradually decreases from 0.2 s to 0.6 s and becomes stable from 0.7 s beyond. Observations in Fig. 11 imply that the microstructure of the bed actually tends to reorganize itself towards a smaller tortuosity and thus a smaller resistance to the fluid flow.

As shown in Fig. 13, particle-particle force chains also witness the microstructural change in the formation of an expanded bed. There are large forces in the initial packed bed ($t = 0$ s), due to the gravitational effect (Yang et al., 2008). At $t = 0.2$ s, the force chains at the bottom becomes much weaker, indicating fluid-induced forces take effect in supporting the bed. Besides, the force chains in the upper region at this stage are relatively strong, implying the history effect that the top of the bed was fallen down from defluidization and enhanced the particle-particle interactions in that region. From 0.2 s to 1.0 s, the force chains become more evenly distributed in the bed. In particular, stronger force chains appear in the bottom region at $t = 1.0$ s, indicating the mechanical strength of the bed structure is improved in this region.

Combining the observations in Figs. (11)–(13), it is known that immediately after flow onset, the gas pressure gradient and drag force rapidly increase, exceeding the effective weight of the particle bed. This excess particle-fluid force produces a sudden reduction in the effective

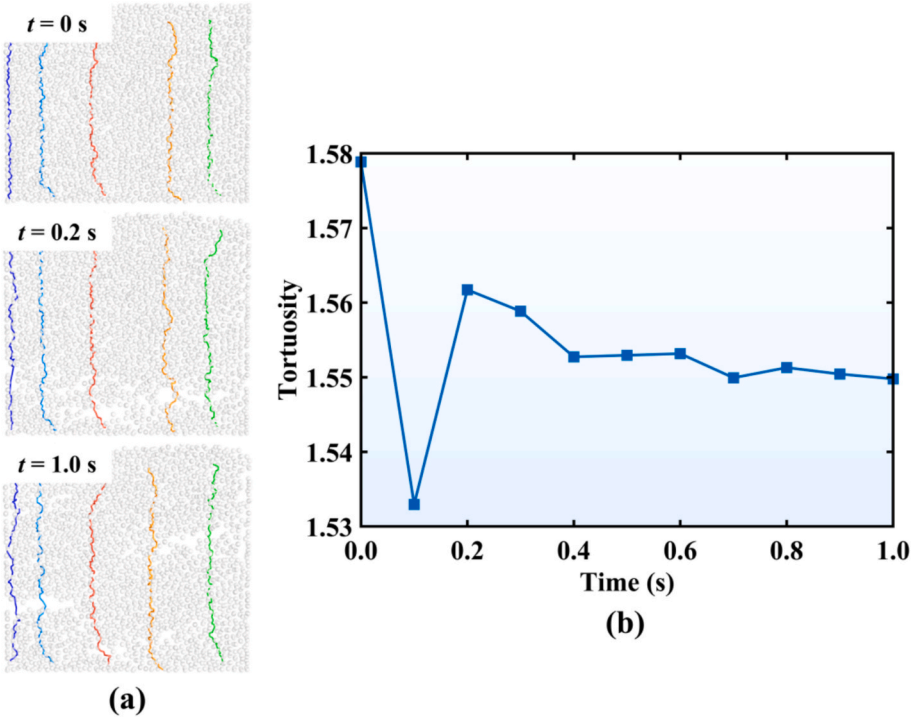

Fig. 12. Torturous flow paths within the bed: (a) typical flow paths; (b) evolution of tortuosity with time.

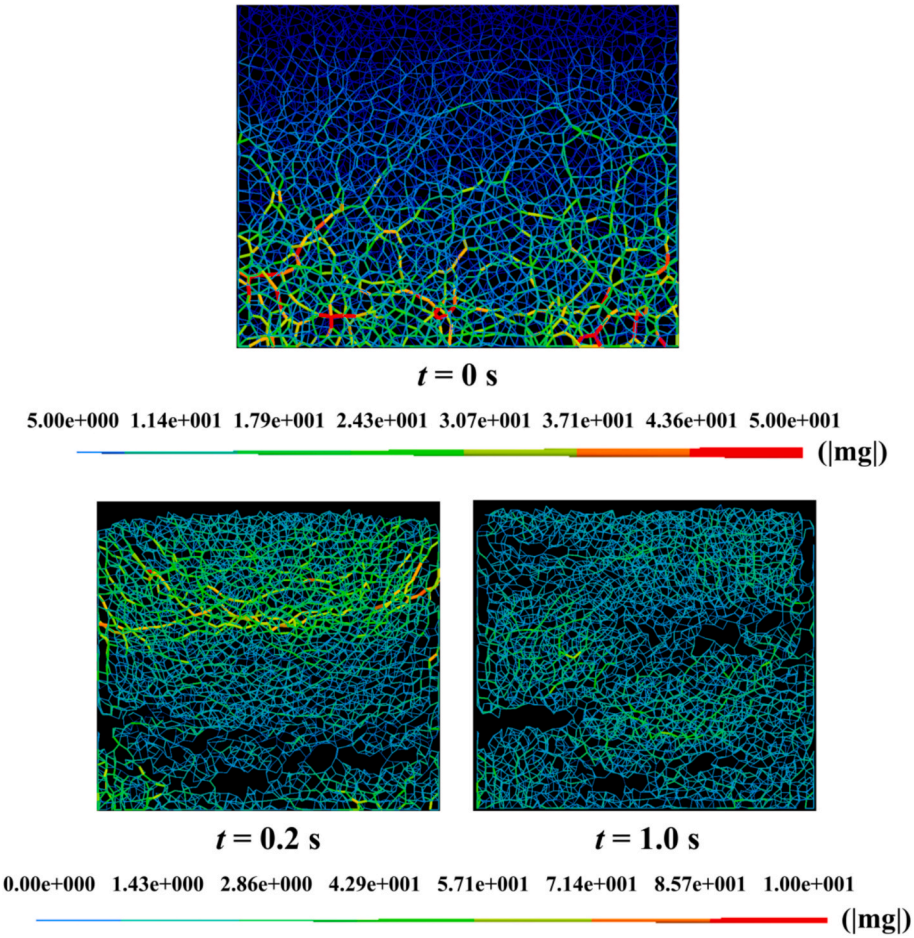

Fig. 13. Evolution of particle contact force chains of the bed, where the stick represents the particle–particle contact pair and the colour/thickness represents the force magnitude.

normal stresses carried by the contact force network. This unloading triggers widespread contact opening and particle-scale dilatancy: force chains buckle and fragment, the coordination number decreases, and particles undergo collective rearrangements that increase local porosity and bed height. As expansion proceeds, a stabilizing feedback mechanism emerges at the microscale, leading to the stable expanded state. The increase in local porosity is not perfectly uniform; instead, the system self-organizes to form micro-channels or preferential flow paths. This structural adjustment allows a significant portion of the gas flux to bypass dense particle clusters, thereby reducing the effective drag force exerted on individual particles. For fine particles, the van der Waals cohesive force acts as a critical "mechanical buffer." It promotes the reformation of enduring contacts and small agglomerates, preventing the complete loss of connectivity. Stability is reached when a delicate three-force balance (particle-fluid force, Van der Waals force and gravity) is re-established. Together with dissipative mechanisms, such as frictional sliding, contact hysteresis, and viscous damping from the interstitial gas, the growth of porosity fluctuations is suppressed. The stable expanded bed is thus a micro-mechanically self-organized state. The transient phase terminates when a dynamically stable microstructure is reached, characterized by stationary contact-force statistics and optimized flow paths, where any further perturbation is dissipated rather than amplified into macroscopic bubbles.

3.3. Correlation of minimum bubbling velocity u_{mb}

In Section 3.2, it is shown a stable expanded bed can be formed at a proper gas velocity. However, if the gas velocity continually increases, the bed will become dynamic and enter the bubbling fluidization region. As mentioned in the Introduction section, prediction on the minimum bubbling velocity (u_{mb}) is consistently studied by researchers, but the consideration of micromechanics at the particle or even pore scale is still lacking. Here, we wish to bridge the connection between the particle-pore scale micromechanics as introduced in Section 3.2 and the prediction on u_{mb}.

First, different particle properties are used to obtain expanded beds and corresponding u_{mb}, as shown in Table 2. Obviously, particle cohesion represented by Hamaker constant (H_a) affects both u_{mb} and the minimum porosity ε_{mb} at the onset of bubbling fluidization. u_{mb} and ε_{mb} generally become higher at a higher H_a. This is because H_a or particle cohesion basically affects the mechanical strength of granular materials. Previously, Rumpf (1962) quantified the tensile strength P_t as a function of particle level cohesion, given as:

$$P_t = \frac{(1-\varepsilon)F_{coh}^{max}CN}{\pi {d_p}^2} \tag{8}$$

where ε is the porosity (equalling ε_{mb} at the onset of bubbling fluidization), F_{coh}^{max} is the maximum cohesion force and can be expressed as $F_{coh}^{max} = H_a d_p/24h_{min}^2$, CN is the particle contact number (or coordination number) for the considered particle assembly; a quantitative relationship between CN and ε in the expanded bed state was previously found (Wu et al., 2017), given as $CN = 2.0 + 26.6\exp(-6\varepsilon)$. Hence, P_t can be explicitly calculated.

Table 2
Minimum bubbling velocity u_{mb} of different material properties.

Case No.	H_a (J)	d_p (um)	ρ_p (kg/m^3)	u_{mb} (cm/s)	ε_{mb}
1	2.10×10^{-21}	96	2460	1.30	0.423
2	2.10×10^{-21}	100	1440	1.00	0.447
3	4.20×10^{-21}	100	1440	1.20	0.469
4	6.50×10^{-21}	100	1440	1.50	0.499
5	6.50×10^{-21}	96	2460	1.80	0.462
6	8.40×10^{-21}	100	1440	1.60	0.514
7	1.05×10^{-20}	100	1440	1.70	0.515
8	1.58×10^{-20}	100	1440	2.00	0.535
9	1.90×10^{-20}	100	1440	2.20	0.543
10	2.10×10^{-20}	100	1440	2.40	0.548
11	4.20×10^{-21}	75	1440	0.90	0.508
12	2.10×10^{-21}	75	1440	0.65	0.460
13	2.10×10^{-21}	50	1440	0.45	0.537
14	4.20×10^{-21}	50	1440	0.60	0.564

For a bubbling fluidization bed, the appearance of dynamic bubbles needs to break those particle assemblies, with the increased particle-fluid force at a high gas velocity (u_{mb}). As indicated by Eq. (4), the particle-fluid interaction will lead to the pressure drop on fluid flow; in turn, the interaction will also result in the particle-fluid force $\mathbf{F}_{pf}$ on particles. With neglecting the inertial flow effect, the following equation is obtained:

$$\frac{\mathbf{F}_{pf}}{A} = \Delta P \ \frac{32\mu L_{i,j}}{D_{i,j}^{*\,2}} U_{i,j} \tag{9}$$

where A is the cross-sectional area of the particle assembly. Normally, $\mathbf{F}_{pf}$ is balanced with the particle weight at a fluidization state. Nevertheless, at the onset or the start-up of bubbling fluidization, $\mathbf{F}_{pf}$ is much larger than the bed weight, as demonstrated in a previous study (Hou et al., 2012). The excessed particle-fluid force possibly plays a role in overcoming the tensile strength P_t of cohesive particles, breaking particle connections for the production of dynamic bubbles. Hence, at the onset of bubbling, $\mathbf{F}_{pf}$ may be balanced with the sum of particle weight and tensile strength of particle assemblies, which can be expressed as:

$$\frac{\mathbf{F}_{pf}}{A} = P_t + P_g \tag{10}$$

where P_g is the particle weight-induced pressure and can be given as $P_g = m_p g/0.25\pi {d_p}^2$. Combing Eqs. (8) and (9), and set $u_{mb} = U_{i,j}$ at the onset of bubbling, the following expression is obtained:

$$u_{mb} = \frac{(\alpha P_t + P_g)\langle D_{throat}\rangle^2}{32\beta\mu\langle L_{thoat}\rangle} \tag{11}$$

where $\langle D_{throat}\rangle$ and $\langle L_{throat}\rangle$ present the mean throat diameter and length of the bed, and a parameter β is incorporated to account for the shape-induced deviation; because the appearance of dynamic bubbles does not require all particle-particle connections to be broken, hence a parameter α is used to consider the partial breakage of particle-particle connections at the onset of bubbling.

Except the fitting parameters α and β, the only unknown variables in *Eq. (10)* are $\langle D_{throat}\rangle$ and $\langle L_{throat}\rangle$. Next, the way to describe the two variables as a function of porosity ε will be proposed. Since the pore unit is composed of four spheres as a tetrahedron (see Fig. 1(c)), we may derive the correlations of $\langle D_{throat}\rangle$ and $\langle L_{throat}\rangle$ from the simple pore unit that the four spheres are at the vertices of a regular tetrahedron (i.e., equal side length for the tetrahedron). Then, a specific side length of the regular tetrahedron l_{tet} corresponds to a specific ε (also D_{throat} and L_{throat}) of the pore unit. Due to the calculation of the solid sphere part within the tetrahedron requires the computation of spherical pyramid, the relationship between l_{tet} and ε (also D_{throat} and L_{throat}) is very complicated and does not have a simple analytical solution. However, we can increase l_{tet} by a small addition each step, and obtain corresponding ε (also D_{throat} and L_{throat}). This can be done by simple programming. As there is one-to-one relationship between l_{tet} and ε (also D_{throat} and L_{throat}), we can express l_{tet} as a function of ε. Similarly, D_{throat} and L_{throat} can also be a function of ε. Thus, the computed results are presented in Fig. 14. Clearly, there are monotonic relationships between porosity and pore structural properties; and quantitative correlations can be obtained by fitting from MATLAB, given as:

$$l_{tet} = 0.988\epsilon^{2.70} + 1 \tag{12}$$

$$D_{throat} = 1.07\epsilon^{1.86} + 0.192 \tag{13}$$

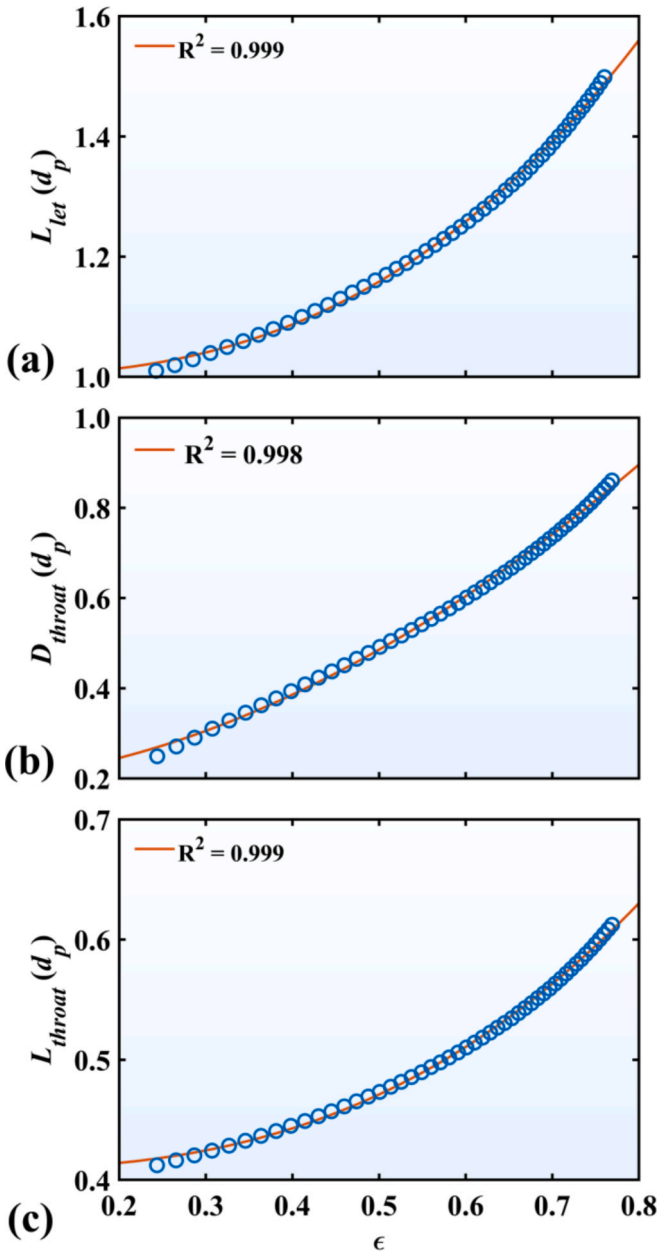

Fig. 14. Correlations between porosity ε and (a) side length l_{tet} of the tetrahedron (four spheres of the pore unit are located at vertices of the tetrahedron), (b) throat diameter D_{throat} and (c) throat length L_{throat}. The red lines in (a), (b) and (c) are given by Eqs. (11)–(13) (R-squared of the fitting are 0.998, 0.998 and 0.989), respectively.

$$L_{throat} = 0.445\epsilon^{2.78} + 0.405 \tag{14}$$

The correlations for throat diameter and length presented in Eqs. (12) and (13) are derived from the geometric evolution of the regular tetrahedron model. Readers should note that these equations are empirical power-law fits intended specifically for the porosity range typical of fixed and stably expanded beds (approximately $0.3 < \varepsilon < 0.7$). Their application should therefore be restricted to the dense-phase fluidization regime analysed in this study.

Based on Eqs. (12) and (13), $\langle D_{throat} \rangle$ and $\langle L_{throat} \rangle$ can be readily obtained using ε_{mb} at the onset of bubbling. Moreover, setting the fitting parameter $\alpha = 0.28$ and $\beta = 8.5$ in *Eq. (10)*, u_{mb} in Table 2 can be well predicted with those material properties, as shown in the Fig. 15.

Therefore, the macroscopic transitional velocity u_{mb} can actually be correlated with the particle-pore scale micromechanics. The derived correlation here has solid physical meanings and explicitly considers the particle scale parameters (e.g., the Hamaker constant for particle cohesion), thus is likely to be more reliable than previous correlations in predicting u_{mb} of fine cohesive particles. Nevertheless, it is subjected to more examinations by experiments in future.

It is important to acknowledge that Eq. (10) relies on microscopic pore geometric parameters, which are currently difficult to measure directly in real-time physical experiments. This limits the feasibility of directly validating the equation against experimental raw data using measured pore inputs. Nonetheless, to confirm the equation's robustness and predictive utility, we performed blind validation tests using additional simulation cases that were not part of the original calibration dataset (Table 2). These independent validation cases, detailed in Table 3, utilize distinct combinations of particle density, size and Hamaker constants to represent a broader range of material properties. As illustrated in Fig. 16, the minimum bubbling velocities predicted by Eq. (10) were compared against the results obtained from these independent DEM-PNM simulations. The comparison still shows a strong agreement, with a relative deviation of less than 10 % for all tested cases. This result confirms that the correlation successfully captures the underlying physics of the cohesive bubbling mechanism and possesses reliable predictive capability for fine particle systems outside the initial parameter space used for regression.

4. Conclusions

A coupled DEM–PNM approach has been developed to simulate particle–fluid flows at equivalent solving scales. The model was evaluated through comparisons with DEM–LBM simulations and applied to investigate the micromechanics of expanded and minimum bubbling fluidization in fine particles. The key findings are as follows:

1) The DEM–PNM approach provides valuable insights into particle–pore scale properties of particle–fluid flows. However, its current applicability is limited to low Reynolds number conditions, as noticeable deviations from DEM–LBM results are observed at higher Reynolds numbers (e.g., Re = 100).
2) The formation of a stable expanded bed of fine particles is successfully reproduced. By characterizing pore-scale fluid flow, flow

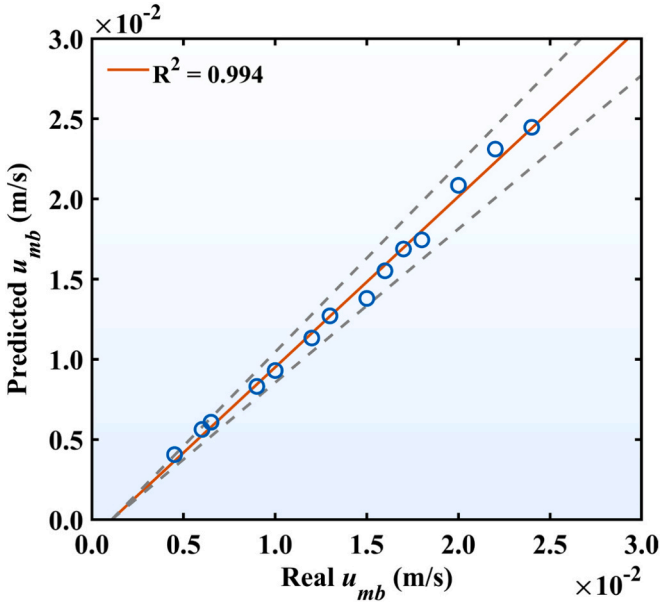

Fig. 15. Real u_{mb} versus predicted u_{mb}, where the dash lines indicate ± 10 % deviation.

Table 3
Predicted and simulated u_{mb} values beyond the calibration domain.

Case No.	H_a (J)	d_p (um)	ρ_p (kg/m^3)	ε_{mb}	u_{mb_pred} (cm/s)	u_{mb_sim} (cm/s)
1	2.1×10^{-21}	45	1600	0.44	0.31	0.34
2	4.2×10^{-21}	55	2800	0.46	1.09	1.04
3	1.5×10^{-21}	70	2000	0.43	0.67	0.71
4	2.5×10^{-20}	90	1500	0.52	1.96	2.08
5	1.0×10^{-20}	110	1800	0.5	2.15	2.02
6	6.5×10^{-21}	60	3000	0.48	1.38	1.46
7	8.4×10^{-21}	40	2200	0.45	0.57	0.62
8	3.0×10^{-20}	80	1700	0.55	1.85	1.74
9	4.2×10^{-21}	95	1400	0.42	1.08	1.14
10	1.2×10^{-20}	65	2600	0.58	1.61	1.52

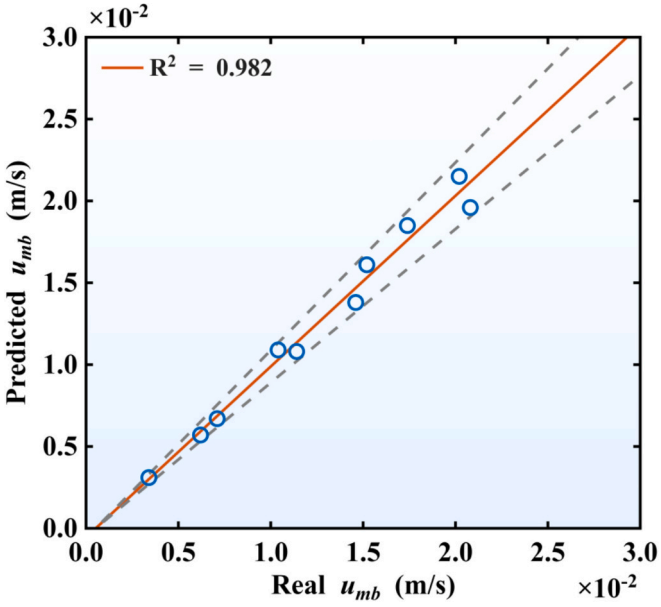

Fig. 16. Real u_{mb} versus predicted u_{mb} using dataset in Table 3, where the dash lines indicate ± 10 % deviation.

tortuosity, and force chains, it is revealed that although macroscopic properties such as bed porosity and pressure drop stabilize quickly after defluidization, the expanded bed still undergoes microscopic structural evolution over a lateral period. These structural adjustments promote reduced resistance to gas flow and enhanced mechanical stability, demonstrating that expanded bed formation is governed by both particle–particle and particle–fluid interactions.

3) By calculating tensile strength with the Rumpf equation (Rumpf, 1962) and quantifying fluid-induced forces at the pore scale, a new correlation is proposed for predicting the minimum bubbling fluidization velocity (u_{mb}) of fine cohesive particles. This correlation explicitly incorporates particle-scale properties and pore structures.

Nonetheless, it should be noted that the model's accuracy is highest in the low Reynolds number regime (Re < 100). The current DEM-PNM model should be used with caution in dilute or high-velocity systems where Re > 100 and inertial effects dominate. Looking ahead, the proposed DEM–PNM framework can be extended to investigate particle–pore scale heat and mass transfer phenomena. Furthermore, its applicability to more complex particle–fluid flow systems at higher Reynolds numbers should be explored.

CRediT authorship contribution statement

Qiong Wu: Writing – original draft, Validation, Methodology, Investigation, Formal analysis. **Yi Zou:** Writing – review & editing, Supervision, Methodology. **Yongli Wu:** Writing – review & editing, Validation, Methodology. **Jing He:** Writing – review & editing, Supervision.

Declaration of competing interest

The authors declare that they have no known competing financial interests or personal relationships that could have appeared to influence the work reported in this paper.

Acknowledgements

The authors are grateful to the financial support from the National Natural Science Foundation of China (No. 52034003 & No. 52006035) and the Natural Science Foundation of Jiangsu Province (No. BK20200269).

Data availability

Data will be made available on request.

References

Al-Gharbi, M.S., Blunt, M.J., 2005. Dynamic network modeling of two-phase drainage in porous media. Phys. Rev. E Stat. Nonlin. Soft Matter Phys. 71, 016308.
Amritkar, A., Deb, S., Tafti, D., 2014. Efficient parallel CFD-DEM simulations using OpenMP. J. Comput. Phys. 256, 501–519.
Blunt, M.J., 2001. Flow in porous media - pore-network models and multiphase flow. Curr. Opin. Colloid Interface Sci. 6, 197–207.
Boissonnat, J.-D., Devillers, O., Pion, S., Teillaud, M., Yvinec, M., 2002. Triangulations in CGAL. Comput. Geom. 22, 5–19.
Bruno, M.S., 1994. Micromechanics of stress-induced permeability anisotropy and damage in sedimentary rock. Mech. Mater. 18, 31–48.
Bryant, S., King, P., Mellor, D., 1993. Network model evaluation of permeability and spatial correlation in a real random sphere packing. Transp. Porous Media 11, 53–70.
Bu, S., Li, D., Chen, S., Xiao, C., Li, Y., 2022. Numerical simulation of landslide-generated waves using a SPH-DEM coupling model. Ocean Eng. 258, 111826.
Cao, Z., Song, Z., Sun, W., Xie, Q., Fumagalli, A., Tian, X., Shen, X., 2025. A numerical approach for CFD-DEM coupling method with pore network model considering the effect of anisotropic permeability in soil-rock mixtures. Comput. Geotech. 178.
Catalano, E., Chareyre, B., Barthélémy, E., 2014. Pore-scale modeling of fluid-particles interaction and emerging poromechanical effects. Int. J. Numer. Anal. Meth. Geomech. 38, 51–71.
Chareyre, B., Cortis, A., Catalano, E., Barthélemy, E., 2011. Pore-scale modeling of viscous flow and induced forces in dense sphere packings. Transp. Porous Media 92, 473–493.
Chen, L., Sun, Z., Ma, H., Pan, G., Li, P., Gao, K., 2022. Flow characteristics of pneumatic conveying of stiff shotcrete based on CFD-DEM method. Powder Technol. 397, 117109.
Cundall, P.A., Strack, O.D.L., 1979. A discrete numerical model for granular assemblies. Géotechnique 29, 47–65.
Fei, L., Qin, F., Wang, G., Huang, J., Wen, B., Zhao, J., Luo, K.H., Derome, D., Carmeliet, J., 2023. Coupled lattice Boltzmann method–discrete element method model for gas–liquid–solid interaction problems. J. Fluid Mech. 975.
Foscolo, P., Gibilaro, L., 1984. A fully predictive criterion for the transition between particulate and aggregate fluidization. Chem. Eng. Sci. 39, 1667–1675.
Fu, S., Su, W., Zhang, H., Wang, L., 2024. An immersed moving boundary for fast discrete particle simulation with complex geometry. Chem. Eng. Sci. 283, 119407.
Fu, S., Wang, L., 2023. GPU-based unresolved LBM-DEM for fast simulation of gas–solid flows. Chem. Eng. J. 465, 142898.
Gan, J., Zhou, Z., Yu, A., 2019. Flow and force analysis on the formation of expanded beds in gas fluidization of fine ellipsoids. Powder Technol. 357, 291–304.
Ge, W., Chang, Q., Li, C., Wang, J., 2019. Multiscale structures in particle–fluid systems: characterization, modeling, and simulation. Chem. Eng. Sci. 198, 198–223.
Geldart, D., 1973. Types of gas fluidization. Powder Technol. 7, 285–292.
Giudici, L.M., Raeini, A.Q., Akai, T., Blunt, M.J., Bijeljic, B., 2023. Pore-scale modeling of two-phase flow: a comparison of the generalized network model to direct numerical simulation. Phys. Rev. E 107, 035107.

Guo, Q., Meng, S., Zhao, Y., Ma, L., Wang, D., Ye, M., Yang, W., Liu, Z., 2018. Experimental Verification of Solid-like and Fluid-like States in the Homogeneous Fluidization Regime of Geldart a Particles. Ind. Eng. Chem. Res. 57, 2670–2686.
Gupta, S., De, S., 2022. An experimental investigation of high-ash coal gasification in a pilot-scale bubbling fluidized bed reactor. Energy 244, 122868.
Hamaker, H.C., 1937. The London—van der Waals attraction between spherical particles. Physica 4, 1058–1072.
Hou, Q.F., Zhou, Z.Y., Yu, A.B., 2012. Micromechanical modeling and analysis of different flow regimes in gas fluidization. Chem. Eng. Sci. 84, 449–468.
Jain, A.K., Juanes, R., 2009. Preferential mode of gas invasion in sediments: grain-scale mechanistic model of coupled multiphase fluid flow and sediment mechanics. J. Geophys. Res. 114.
Jendersie, R., Mjalled, A., Lu, X., Reineking, L., Kharaghani, A., Mönnigmann, M., Lessig, C., 2024. NeuroPNM: model reduction of pore network models using neural networks. Particuology 86, 239–251.
Ji, L., Paul, P., Shanbhag, B.K., Dixon, I., Kuang, S., He, L., 2023. Emerging application of hydrocyclone in biotechnology and food processing. Sep. Purif. Technol. 309, 122992.
Jiang, F., Liu, H., Chen, X., Tsuji, T., 2022. A coupled LBM-DEM method for simulating the multiphase fluid-solid interaction problem. J. Comput. Phys. 454, 110963.
Jo, Y.B., Park, S.-H., Yoo, H.S., Kim, E.S., 2022. GPU-based SPH-DEM method to examine the three-phase hydrodynamic interactions between multiphase flow and solid particles. Int. J. Multiph. Flow 153, 104125.
Kloss, C., Goniva, C., Hager, A., Amberger, S., Pirker, S., 2012. Models, algorithms and validation for opensource DEM and CFD–DEM. Prog. Comput. Fluid Dyn.An Int. J. 12, 140–152.
Li, M., Wu, J., Li, J., Zhuang, L., Wang, S., Zhang, F., 2022. Modeling of hydraulic fracturing in polymineralic rock with a grain-based DEM coupled with a pore network model. Eng. Fract. Mech. 275.
Liu, D., Bu, C., Chen, X., 2013. Development and test of CFD–DEM model for complex geometry: a coupling algorithm for Fluent and DEM. Comput. Chem. Eng. 58, 260–268.
Liu, X., Ge, W., Wang, L., 2020. Scale and structure dependent drag in gas–solid flows. AIChE J 66, e16883.
Ma, T., Yu, Y., Chen, X., Zhou, Q., 2020. Effect of anisotropic microstructures on fluid-particle drag in low-Reynolds-number monodisperse gas-solid suspensions. AIChE J 66, e16910.
Menon, N., Durian, D.J., 1997. Particle motions in a gas-fluidized bed of sand. Phys. Rev. Lett. 79, 3407–3410.
Mufti, S., Das, A., 2023. Multiscale pore network construction for two phase flow simulations in granular soils. Advances in Water Resources 173.
Oke, O., Lettieri, P., Mazzei, L., 2015. An investigation on the mechanics of homogeneous expansion in gas-fluidized beds. Chem. Eng. Sci. 127, 95–105.
Qi, Z., Kuang, S., Rong, L., Yu, A., 2018. Lattice Boltzmann investigation of the wake effect on the interaction between particle and power-law fluid flow. Powder Technol. 326, 208–221.
Qi, Z., Kuang, S., Yu, A., 2019. Lattice Boltzmann investigation of non-Newtonian fluid flow through a packed bed of uniform spheres. Powder Technol. 343, 225–236.
Rhodes, M.J., Wang, X.S., Nguyen, M., Stewart, P., Liffman, K., 2001. Use of discrete element method simulation in studying fluidization characteristics: influence of interparticle force. Chem. Eng. Sci. 56, 69–76.
Rong, L.W., Dong, K.J., Yu, A.B., 2013. Lattice-Boltzmann simulation of fluid flow through packed beds of uniform spheres: effect of porosity. Chem. Eng. Sci. 99, 44–58.
Rong, L.W., Dong, K.J., Yu, A.B., 2020. Lattice-Boltzmann computation of hydraulic pore-to-pore conductance in packed beds of uniform spheres. Chem. Eng. Sci. 224.
Rumpf, H., 1962. The strength of granules and agglomerates. Agglomeration 379–418.
Rycroft, C.H., 2009. VORO++: a three-dimensional voronoi cell library in C++. Chaos 19, 041111.
Shi, Q., Sakai, M., 2022. Recent progress on the discrete element method simulations for powder transport systems: a review. Adv. Powder Technol. 33, 103664.
Sufian, A., Knight, C., O'Sullivan, C., van Wachem, B., Dini, D., 2019. Ability of a pore network model to predict fluid flow and drag in saturated granular materials. Comput. Geotech. 110, 344–366.
Sundaresan, S., Ozel, A., Kolehmainen, J., 2018. Toward constitutive models for momentum, species, and energy transport in gas-particle flows. Annu. Rev. Chem. Biomol. Eng. 9, 61–81.
Tang, Y., Lau, Y.M., Deen, N.G., Peters, E.A.J.F., Kuipers, J.A.M., 2016. Direct numerical simulations and experiments of a pseudo-2D gas-fluidized bed. Chem. Eng. Sci. 143, 166–180.
Tang, H., Song, R., Dong, Y., Song, X., 2019. Measurement of Restitution and Friction Coefficients for Granular Particles and Discrete Element Simulation for the Tests of Glass Beads. Materials 3170.
Thompson, K.E., Fogler, H.S., 1997. Modeling flow in disordered packed beds from pore-scale fluid mechanics. AIChE J 43, 1377–1389.
Thornton, C., Yang, F., Seville, J., 2015. A DEM investigation of transitional behaviour in gas-fluidised beds. Powder Technol. 270, 128–134.
Tsigginos, C., Meng, J., Gu, X.-J., Emerson, D.R., 2022. Coupled LBM-DEM simulations using the partially saturated method: Theoretical and computational aspects. Powder Technol. 405, 117556.
Valverde, J.M., Castellanos, A., Mills, P., Quintanilla, M.A.S., 2003. Effect of particle size and interparticle force on the fluidization behavior of gas-fluidized beds. Phys. Rev. E Stat. Nonlinear Soft Matter Phys. 67, 051305.
van der Hoef, M.A., van Sint Annaland, M., Deen, N.G., Kuipers, J.A.M., 2008. Numerical simulation of dense gas-solid fluidized beds: a multiscale modeling strategy. Annu. Rev. Fluid Mech. 40, 47–70.
Wang, J., van der Hoef, M.A., Kuipers, J.A.M., 2010. CFD study of the minimum bubbling velocity of Geldart a particles in gas-fluidized beds. Chem. Eng. Sci. 65, 3772–3785.
Wang, S., Hu, C., Luo, K., Yu, J., Fan, J., 2023. Multi-scale numerical simulation of fluidized beds: Model applicability assessment. Particuology 80, 11–41.
Wang, S., Shen, Y., 2021a. CFD-DEM modelling of raceway dynamics and coke combustion in an ironmaking blast furnace. Fuel 302.
Wang, S., Shen, Y., 2021b. Particle-scale modelling of raceway dynamics in a blast furnace using a smoothing method. Powder Technol. 389, 189–203.
Wang, S., Shen, Y., 2022. Coarse-grained CFD-DEM modelling of dense gas-solid reacting flow. Int. J. Heat Mass Transf. 184, 122302.
Wen, C.Y., Yu, Y.H., 1966. A generalized method for predicting the minimum fluidization velocity. AIChE J 12, 610–612.
Wu, Y.L., Hou, Q.F., Yu, A.B., 2017. Particle-scale study of structural transition of solid phase in gas-fluidized beds. Ind. Eng. Chem. Res. 56, 5455–5468.
Wu, Y.L., Hou, Q.F., Yu, A.B., 2019. Pore-scale study of fluid flow and drag force in randomly packed beds of different porosities. Ind. Eng. Chem. Res. 58, 5041–5053.
Xu, W.-J., Zhou, Q., Dong, X.-Y., 2022. SPH–DEM coupling method based on GPU and its application to the landslide tsunami. Part II: reproduction of the Vajont landslide tsunami. Acta Geotech. 17, 2121–2137.
Yang, R.Y., Zou, R.P., Yu, A.B., 2000. Computer simulation of the packing of fine particles. Phys. Rev. E 62, 3900–3908.
Yang, R.Y., Zou, R.P., Yu, A.B., Choi, S.K., 2008. Characterization of interparticle forces in the packing of cohesive fine particles. Phys. Rev. E 78, 031302.
Yang, Z., Juanes, R., 2018. Two sides of a fault: Grain-scale analysis of pore pressure control on fault slip. Phys. Rev. E 97, 022906.
Ye, M., van der Hoef, M.A., Kuipers, J.A.M., 2004. A numerical study of fluidization behavior of Geldart a particles using a discrete particle model. Powder Technol. 139, 129–139.
Yue, Y., Zhang, C., Shen, Y., 2021. CFD-DEM model study of gas–solid flow in a spout fluidized bed with an umbrella-like baffle. Chem. Eng. Sci. 230.
Zhang, F., Damjanac, B., Huang, H., 2013. Coupled discrete element modeling of fluid injection into dense granular media. J. Geophys. Res. Solid Earth 118, 2703–2722.
Zhao, J., Liu, Y., Qin, F., Fei, L., 2023. Pore-scale fluid flow simulation coupling lattice Boltzmann method and pore network model. Capillarity 7, 41–46.
Zhou, Q., Xu, W.-J., Dong, X.-Y., 2022. SPH-DEM coupling method based on GPU and its application to the landslide tsunami. Part I: method and validation. Acta Geotech. 17, 2101–2119.
Zhu, H.P., Zhou, Z.Y., Yang, R.Y., Yu, A.B., 2007. Discrete particle simulation of particulate systems: theoretical developments. Chem. Eng. Sci. 62, 3378–3396.
Zou, L., Sun, J.Z., Sun, Z., Yu, Z.B., Zhao, H.B., 2022. Study of two free-falling spheres interaction by coupled SPH–DEM method. Eur. J. Mech. A Solids 92, 49–64.